










## RESEARCH ARTICLE OPEN ACCESS

# Noble Metal-Based High Entropy Alloy Nanoparticles Prepared by Pulsed Electrodeposition: An Approach for Medium Throughput Studies

Divyansh Gautam<sup>1</sup>  | Gustav K. H. Wiberg<sup>1,2</sup>  | Jonathan Quinson<sup>3</sup>  | Di Wang<sup>4</sup> | Christian M. Clausen<sup>5</sup>  | Rasmus Rohde<sup>6</sup>  | Rebekka Klemmt<sup>6</sup>  | Jan Rossmeisl<sup>5</sup>  | Espen Drath Bojesen<sup>6</sup>  | Matthias Arenz<sup>1</sup> 

<sup>1</sup>Department of Chemistry, Biochemistry and Pharmaceutical Sciences, University of Bern, Bern, Switzerland | <sup>2</sup>Department of Physics, University of Nevada, Reno, USA | <sup>3</sup>Biological and Chemical Engineering, Aarhus University, Aarhus, Denmark | <sup>4</sup>Institute of Nanotechnology and Karlsruhe Nano Micro Facility (KNMF), Karlsruhe Institute of Technology (KIT), Eggenstein-Leopoldshafen, Germany | <sup>5</sup>Department of Chemistry, University of Copenhagen, Copenhagen, Denmark | <sup>6</sup>Center for Sustainable Energy Materials (CENSEMAT), Department of Chemistry and Interdisciplinary Nanoscience Center (iNANO), Aarhus University, Aarhus, Denmark

**Correspondence:** Matthias Arenz ([matthias.arenz@unibe.ch](mailto:matthias.arenz@unibe.ch))

**Received:** 23 September 2025 | **Revised:** 10 November 2025 | **Accepted:** 19 November 2025

**Keywords:** electrocatalysis | electrodeposition | high entropy alloys

## ABSTRACT

We present a medium-throughput synthesis approach for High Entropy Alloy (HEA) noble metal nanoparticles on conductive supports via electrodeposition. The presented method utilizes aqueous electrolyte solutions, exploiting high overpotentials to achieve mass transport-controlled deposition. This ensures electrodeposition independent from individual equilibrium potentials of the different elements. Hydrogen evolution which interferes with electrodeposition is suppressed by operating in a pulsed mode at a mildly acidic pH. Applying the approach to the Au–Ir–Pt–Pd–Rh–Ru composition space, this study demonstrates that the developed method is fast, adaptable, and enables compositional control while maintaining a homogeneous element distribution. The mechanism of HEA nanoparticle synthesis is further investigated by examining material-specific seed formation and diffusion phenomena. The results indicate that together with the electrolyte composition, seed formation as well as the diffusion of metal precursors in the aqueous phase govern the average composition of the synthesized HEA nanoparticles, while the formation enthalpies of element pairs explain the atomic-scale segregation observed.

## 1 | Introduction

Cantor, as well as Yeh and colleagues, independently introduced the concept of High Entropy Alloys (HEAs) by combining five or more elements in concentrations of 5–35 atomic percent (at%) into a single crystallographic phase, which enhances configurational entropy and stabilizes metastable, disordered phases [1, 2]. This concept has spurred significant research into HEAs for structural and engineering applications [3–6]. More recently, HEAs have also emerged as promising material platform for electrocatalytic reactions such as oxygen reduction, oxygen evolution, hydrogen oxidation, and CO oxidation [7–13]. Their vast

compositional space enables precise tuning of catalytic properties by adjusting elemental composition, thus offering the potential to optimize activity, selectivity, and stability [14]. Initially, research related to HEA catalysis focused on individual HEA compositions, but it was later recognized that HEAs could serve as a broader platform for catalyst discovery—extending beyond traditional HEAs to include alloys with fewer components that are not strictly defined as HEAs but are outer positions, for example, edges, of the multi-dimensional HEA composition space [10–12]. By synthesizing thin-film material libraries and employing density functional theory (DFT), researchers have developed high-throughput protocols to

This is an open access article under the terms of the [Creative Commons Attribution](https://creativecommons.org/licenses/by/4.0/) License, which permits use, distribution and reproduction in any medium, provided the original work is properly cited.

© 2025 The Author(s). *Small Structures* published by Wiley-VCH GmbH.

explore trends in catalytic activity for various reactions [9, 15–17]. However, navigating the vast compositional space of HEAs for catalytic applications remains a challenge due to the sheer number of possible material combinations. When focusing on HEA nanoparticles - the industrially preferred catalytic form compared to thin films - the complexity further increases [13, 18]. Establishing high-throughput synthesis platforms with precise control over material properties is difficult, leading most studies to focus on only a small set of HEA nanoparticle compositions. Thus, a key challenge remains: establishing synthesis methods that allow reproducible and predictable control over HEA nanoparticle properties within complete composition spaces and that at the same time enable a reasonable sample throughput.

Because they contain multiple elements, HEAs are prone to phase separation and compositional ordering, leading to element-segregated surfaces. This not only makes predictions of catalytic behavior more difficult but also hampers rational analysis or approaches such as projecting properties from higher to lower dimensions, that is, from many to fewer alloying components [19]. To establish systematic correlations between nominal composition and catalytic activity, reproducible synthesis methods are required ensuring uniform elemental distribution while maintaining medium-throughput capabilities. Furthermore, understanding chemical ordering tendencies within HEA nanoparticles is critical, as atomic-level compositional fluctuations can introduce active site inhomogeneity, potentially affecting both catalytic activity and stability [20–23]. Therefore, once optimal composition ranges are identified, advanced characterization techniques such as high-resolution scanning transmission electron microscopy (HR-STEM), and synchrotron-based X-ray scattering become essential for probing atomic-scale order-disorder phenomena.

As outlined above, developing synthesis methods for HEA nanoparticles with high reproducibility and precise compositional control is essential for addressing these challenges. A variety of top-down and bottom-up approaches have been explored for multimetallic nanoparticle synthesis, including solvothermal, hot injection, and microwave-assisted methods, each with distinct advantages and limitations [13, 24–28]. Table S1 in the Supporting Information compares various nanoparticle synthesis methods and thin-film libraries, outlining their strengths and limitations. Electrodeposition, by comparison, is substantially less studied, despite the fact that it is an established method for nanoparticle synthesis. Electrodeposition potentially offers rapid, room-temperature fabrication directly on conductive supports [29]. Nevertheless, electrodeposition so far has been primarily used for multielement thin films, with limited exploration of its capability to generate diverse HEA nanoparticle compositions [30]. Therefore, in this work, we aimed to develop a versatile electrochemical HEA nanoparticle synthesis method applicable to various carbon supports commonly used in electrocatalysis, such as glassy carbon (GC), high-surface-area supports, and gas diffusion layers (GDLs). Our goal was also to reduce sample preparation time, enabling a medium-throughput strategy for producing multiple HEA samples efficiently. In our work, aqueous electrolyte solutions were used, which are considered ‘green solvents’ and facilitate the deposition of transition metals. Potentially, the use of organic solvents could enable the deposition of a broader range of materials, including refractory metals.

In previous studies, potentiostatic or galvanostatic biasing has been employed to synthesize multielement films [31]. However, steady-state conditions and moderate overpotentials can lead to kinetic as well as diffusion limitations, particularly for metal cations with slower diffusion rates. To overcome these challenges, we implemented a pulsed electrodeposition strategy with low metal ion concentration in the electrolyte and high overpotentials. The use of high overpotentials ensures electrodeposition independent of individual equilibrium potentials of specific elements, while intermittent pauses allow metal ions to diffuse toward the electrode interface. Additionally, electrodeposition is initiated by a seeding pulse, which generates nucleation sites on the substrate surface, promoting uniform nanoparticle growth [32]. Finally, hydrogen evolution is suppressed by operating at a mildly acidic pH. To validate our approach, we investigated the homogeneity of as-synthesized Au–Ir–Pt–Pd–Rh–Ru nanoparticles including subspaces, examining both global (mesoscale) and local (nanoscale and atomic-scale) compositions using electron microscopy coupled with energy-dispersive X-ray spectroscopy (EDX). Furthermore, to demonstrate medium-throughput capabilities, we synthesized a library of 20 different compositions and analyzed the controllability of the resulting elemental distributions. The importance of seed formation was explored through monometallic depositions, revealing that incorporating a diffusion adjustment factor on bulk electrolyte composition enables accurate prediction of obtained particle compositions. Lastly, we discuss short-range compositional ordering and atomic scale inhomogeneities using computed formation energies (FE) from DFT calculations.

## 2 | Results and Discussion

### 2.1 | Pulsed Electrodeposition Approach

A schematic overview of the pulsed electrodeposition approach is presented in Figure 1, while the electrochemical cell with a three-electrode assembly is shown in Figure S1. The synthesis begins with the insertion of the working electrode at  $E_{\text{insertion}}$ , a potential chosen to prevent spontaneous metal deposition, which can otherwise occur under open circuit potential (OCP). The electrodeposition sequence typically starts with a seeding pulse, initiating nucleation of metal particles on the substrate, followed by alternating potential steps between a rest potential ( $E_{\text{rest}}$ ), allowing diffusion of metal cations from the bulk electrolyte to the electrode surface, and a deposition potential ( $E_{\text{deposition}}$ ), sufficient to quickly reduce all metal ions under mass transport limitation. The optimal deposition scheme is tunable and depends on the specific metal precursor mix. In this study, optimal parameters were determined through potential hold experiments using several different metal precursors, followed by characterization via scanning electron microscopy (SEM)-EDX (see Figure S2 for representative data). By adjusting the sequence, parameters such as particle size and particle density can be varied. For the Au–Ir–Pt–Pd–Rh–Ru system, optimal conditions involved micromolar metal ion concentrations, slightly acidic pH, and deposition potentials just positive of the reversible hydrogen electrode (RHE) to avoid hydrogen evolution. As shown in Figures 1C–E and 2, these conditions yielded Ir–Pt–Pd–Rh–Ru well-defined HEA nanoparticles. Furthermore, the approach is compatible with various conductive substrates,

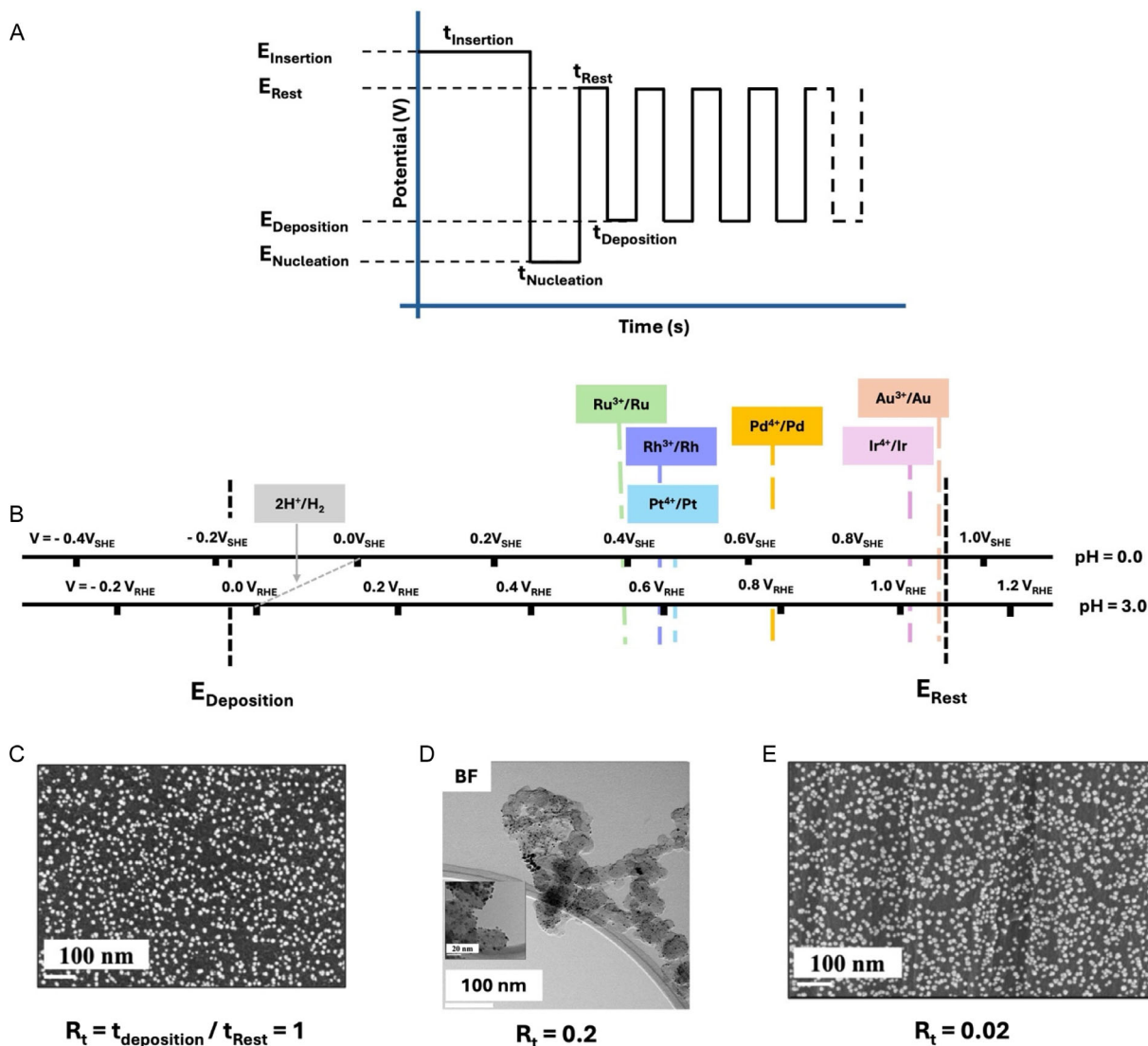


**FIGURE 1** | Summary of synthesis approach. (A) Potential pulse scheme. (B) Chosen values for  $E_{\text{deposition}}$  and  $E_{\text{rest}}$  on RHE scale, along with the representative redox potentials of the used noble metals at SHE and RHE scales. (C) Illustrative scanning electron microscopy (SEM) micrographs of HEA nanoparticles deposited onto a glassy carbon surface. (D) Bright field (BF) transmission electron microscopy (TEM) image of HEA nanoparticles deposited onto high surface area carbon (Ketjen black). (E) SEM micrograph of HEA nanoparticles deposited onto gas diffusion layer (GDL) fibers.

including GC, high-surface-area carbon (Ketjen Black, KB), and GDLs. Uniform nanoparticle distributions were obtained on all substrates (Figure 1). The optimal ratio of duration of potential holds at  $E_{\text{deposition}}$  ( $t_{\text{deposition}}$ ) and  $E_{\text{rest}}$  ( $t_{\text{rest}}$ ), that is,  $R_t = t_{\text{deposition}}/t_{\text{rest}}$ , thereby varies depending on the substrate type. For porous substrates such as GDLs, longer diffusion times are required compared to flat substrates like GC surfaces. For example, on GC, a  $R_t$  of 1.0 resulted in a uniform distribution of nanoparticles with typical sizes between 5 and 30 nm, see also supporting information, while on GDLs an  $R_t$  of 0.02 was required to yield a uniform layer of 10–25 nm nonagglomerated particles. On KB, an  $R_t$  of 0.2 produced well-defined 6–8 nm particles, avoiding agglomeration.

In Figure 2, we first discuss an example from the Ir–Pt–Pd–Rh–Ru subspace, that is, without Au. The STEM-EDX and X-ray total scattering characterization of the nanoparticles indicates the formation of a single crystallographic phase with homogeneous elemental distribution. The nanoparticles were deposited onto

GDLs and transferred to transmission electron microscopy (TEM) grids for STEM-EDX analysis. EDX revealed compositions of Ir ( $22.6 \pm 2.1$  at%), Pt ( $23.2 \pm 1.8$  at%), Pd ( $19.7 \pm 4.2$  at%), Ru ( $11.8 \pm 1.2$  at%), and Rh ( $22.3 \pm 2.0$  at%), that is,  $\text{Ir}_{23}\text{Pt}_{23}\text{Pd}_{20}\text{Ru}_{12}\text{Rh}_{22}$ , see Figure S3 for EDX spectra. The scattering data confirmed the formation of face-centered cubic (FCC) nanoparticles with an average lattice parameter of  $3.858 \text{ \AA}$  and a spherical amplitude correction of  $7.14 \text{ nm}$ . Additionally, the lattice parameter from the selected area electron diffraction (SAED) pattern was determined to be  $3.822 \pm 0.011 \text{ \AA}$ , as shown in Figure S4. The lower observed FCC lattice parameter with respect to pure Pt ( $3.924 \text{ \AA}$ ) obtained by both methods is indicative of compressive strain.

## 2.2 | Exploring HEA Composition Spaces

Having demonstrated the formation of well-defined, single-phase HEA nanoparticles via our electrodeposition approach, we address the next major challenge: the systematic exploration

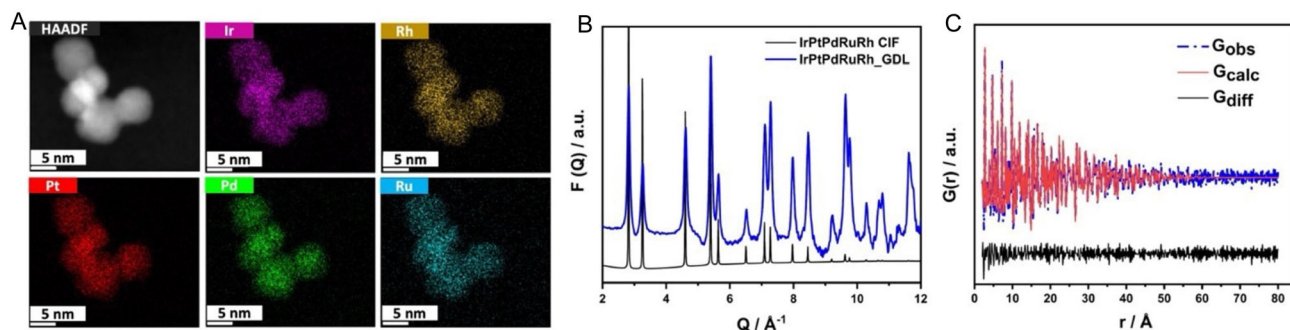


**FIGURE 2** | Characterization of Ir–Pt–Pd–Ru–Rh nanoparticles electrodeposited onto GDL fibers. The composition of the sample as determined by EDX is: Ir ( $22.6 \pm 2.1$ ), Pt ( $23.2 \pm 1.8$ ), Pd ( $19.7 \pm 4.2$ ), Ru ( $11.8 \pm 1.22$ ), Rh ( $22.3 \pm 2.04$ ). (A) HAADF image (collected from Talos microscope) of Ir–Pt–Pd–Ru–Rh NPs along with EDX maps of the different elements. (B) Reduced structure function in reciprocal space acquired from total scattering data and (C) correspond to reduced pair distribution function in real space. The synthesis protocol was as follows: The working electrode was held at  $E_{insertion} = 1.2 V_{RHE}$  for 2 min, before applying a nucleation pulse ( $E_{nucleation}$ ) at  $-0.10 V_{RHE}$  for 2 s. Then a pulsed electrodeposition protocol was applied with  $E_{deposition} = -0.05 V_{RHE}$  of  $t_{deposition} = 0.2$  s and  $E_{rest} = 1.15 V_{RHE}$  of  $t_{rest} = 10$  s for total duration of 1 h. Concentration of precursors:  $Ir^{4+}$  - 150  $\mu M$ ,  $Pt^{4+}$  - 85  $\mu M$ ,  $Pd^{4+}$  - 85  $\mu M$ ,  $Ru^{3+}$  - 85  $\mu M$ ,  $Rh^{3+}$  - 100  $\mu M$ .

of compositional spaces. A key difficulty lies in efficiently navigating composition spaces, that is, transitioning between compositions and adjusting dimensionality (e.g., by adding/removing elements) without significantly altering the structural properties of the HEA nanoparticles [8, 19, 33]. We first describe how to predict the obtained nanoparticle composition based on precursor concentrations and ion-specific mass transport properties, before demonstrating how to alter compositional dimensionality. Accurate prediction of the obtained nanoparticle composition is crucial for optimization strategies such as Bayesian optimization, which rely on balancing exploration and exploitation when proposing new compositions [10, 11].

To enable reproducible synthesis of targeted compositions, we studied the correlation between bulk electrolyte composition and resulting nanoparticle composition synthesized on GC, using SEM-EDX to measure the average composition at a scale of 10–500 nm, referred to as mesoscale composition. This analysis involved 21 syntheses using distinct precursor mixtures in the Au–Ir–Pt–Pd–Rh–Ru system (Table S2). Introducing Au into multimetallic nanoparticles presents challenges, as significant differences in reduction kinetics and diffusion rates often lead to phase-segregated structures in temperature-driven syntheses. For example, Schneider et al. observed phase separation in Ir–Pt–Cu–Au–Ag thin films due to variations in activation energy barriers for surface diffusion [34]. Despite these challenges, incorporating Au into HEA nanoparticles is of high interest as it can enhance the electrochemical stability of alloy nanoparticles and, in some cases, even improve catalytic activity in electrochemical reactions [35]. Herein, synthesis was focused on GC due to faster synthesis time ( $R_t = 1$ , total duration of synthesis 90 s) than that on GDL or KB (refer to Methods), making GCs suitable for faster screening. The nanoparticles were collected from the GC substrates by ultrasonication and transferred to TEM grids. EDX spectra were recorded on several agglomerates for statistical accuracy (Table S3–4). Sample synthesized on GC were also imaged under SEM to capture micrographs which were further used to estimate the average particle size. Figure S5 shows the segmentation performed using watershed algorithm to get distribution of particle size from a single gray-scale image. Table S5 summarizes the weighted mean and weighted standard

deviations for all the 21 samples prepared. As shown in the parity plot (Figure 3A), an overall correlation between electrolyte and nanoparticle composition exists, but composition-dependent deviations complicate precise predictions. To address this, we introduced a diffusion-based adjustment factor,  $(B/z)$ , where  $B$  is the experimentally determined Levich constant, and  $z$  is the metal ion charge. This adjustment is based on the assumption that under mass transport control, deposition rates are governed by diffusion constants leading to well-defined diffusion-limited deposition currents  $I_L$ , (see Levich equation, Equation S1).  $B$  values were extracted from monometallic electrodepositions at varying rotation rates (Figures S6), yielding:  $-43.6$ ,  $-18.5$ ,  $-43.3$ ,  $-23.8$ ,  $-24.2$ , and  $-12.9 \mu A/Hz^{1/2}$  for  $Au^{3+}$ ,  $Ir^{4+}$ ,  $Pt^{4+}$ ,  $Pd^{4+}$ ,  $Rh^{3+}$ , and  $Ru^{3+}$ , respectively (Figure S7). Interestingly,  $Au^{3+}$ ,  $Pt^{4+}$ ,  $Pd^{4+}$ , and  $Rh^{3+}$  showed diffusion-limited behavior at  $-0.05 V_{RHE}$ , while  $Ir^{4+}$  and  $Ru^{3+}$  exhibited mixed kinetic-diffusion control. In fact, electrodeposition of  $Ir^{4+}$  or  $Ru^{3+}$  metal precursors alone yielded no metallic deposits, suggesting a co-reduction mechanism enables the incorporation of Ir and Ru into the HEA nanoparticles by early nucleation of more reducible species such as Au or Pt (Figure S8).

As demonstrated in Figure 3B, applying the  $(B/z)$  adjustment significantly improves prediction accuracy (refer to section Diffusion Adjustment in the Supporting Information, Table S6). With the diffusion adjustment, the mean absolute errors (MAEs) between predicted and obtained composition decrease across all elements. Moreover, compositional distances measured between the mesoscale (10–500 nm) composition and the electrolyte composition were found to decrease after diffusion adjustment on the bulk electrolyte composition (Figure S9). It should be mentioned though that some exceptions - such as the equimolar Pt–Rh system (Table S7), showed no improvement or slight under-correction. However, this was typically the case when the initial prediction was already accurate. In summary, the diffusion adjustment enhances predictability of the obtained nanoparticle composition, though direct composition analysis remains essential.

We further demonstrate the change of HEA composition space dimensionality by synthesizing Au–Pt–Pd–Rh, Au–Ir–Pt–Pd–Rh, and Au–Ir–Pt–Pd–Rh–Ru nanoparticles, see Figure 4. The different nanoparticles exhibit compositional homogeneity and



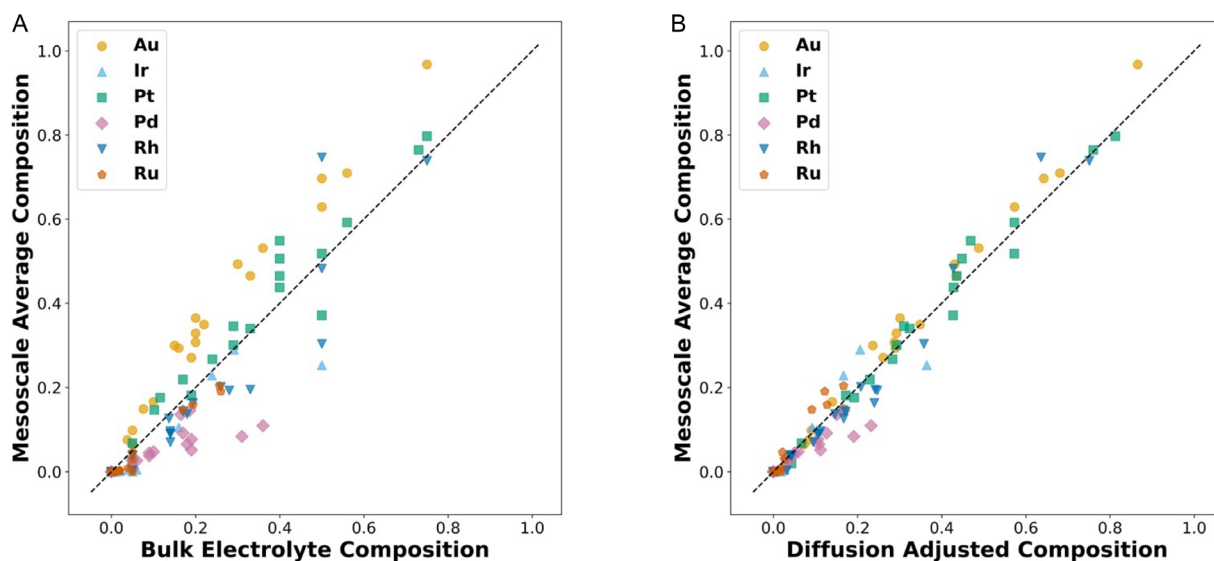


**FIGURE 3** | (A,B) Shows parity plots of the bulk electrolyte compositions and diffusion corrected compositions with respect to the mesoscale average (Aitchison Mean) EDX compositions found in 21 different samples synthesized by electrodeposition.

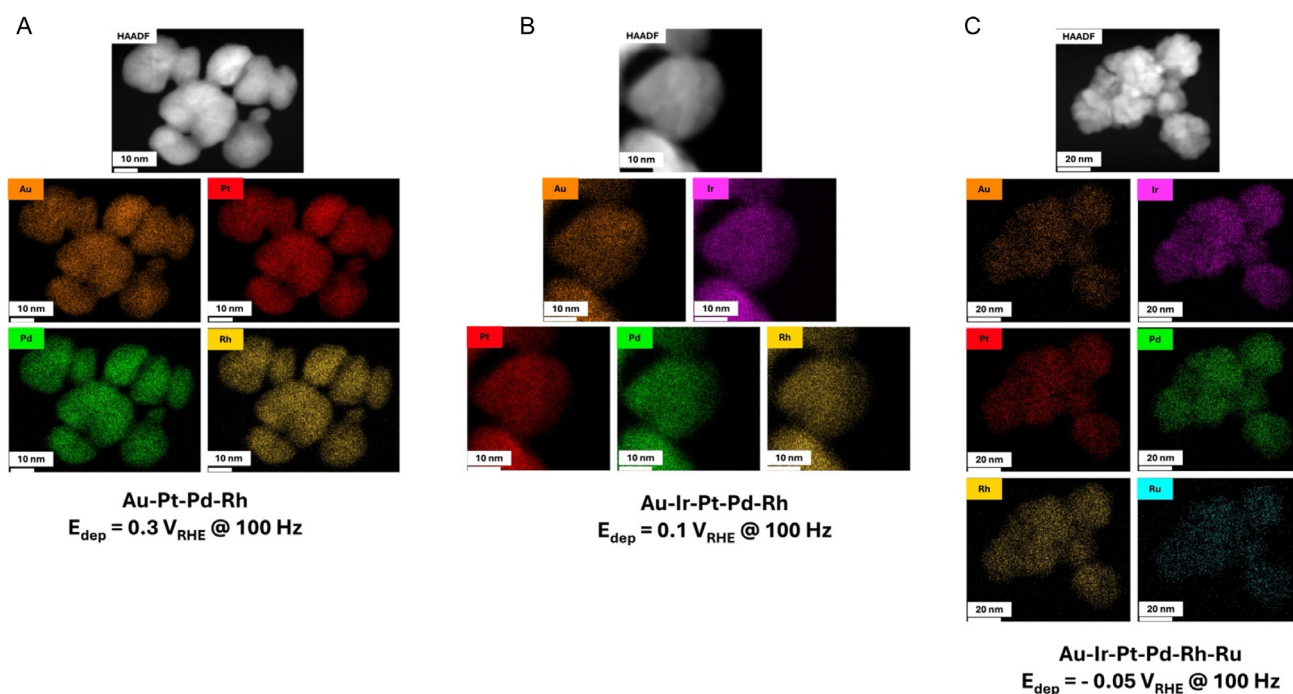


**FIGURE 4** | Adjusting the dimensionality of the composition space of HEA nanoparticles. (A) Au-Pt-Pd-Rh nanoparticles, (B) Au-Ir-Pt-Pd-Rh nanoparticles, and (C) Au-Ir-Pt-Pd-Rh-Ru nanoparticles prepared on GC. For the prepared deposition potential  $E_{\text{deposition}}$  has been adjusted from  $0.3 V_{\text{RHE}}$  to  $0.1 V_{\text{RHE}}$  and  $-0.05 V_{\text{RHE}}$ , respectively, to account for the different deposition kinetics of the metal precursors. After 2 min of  $E_{\text{insertion}}$  of  $1.2 V_{\text{RHE}}$ , an  $E_{\text{nucleation}}$  at  $-0.1 V_{\text{RHE}}$  for 2 s was used. After nucleation pulse, two potential pulses were used,  $1.1 V_{\text{RHE}}$  ( $E_{\text{rest}}$ ) and different  $E_{\text{dep}}$  as mentioned above with a pulsing frequency ( $R_t = 1.0$ ; 100 Hz) were applied for 90 s. For the synthesis, the precursor concentrations were:  $\text{Au}^{3+}$  - 20  $\mu\text{M}$ ,  $\text{Ir}^{4+}$  - 150  $\mu\text{M}$ ,  $\text{Pt}^{4+}$  - 60  $\mu\text{M}$ ,  $\text{Pd}^{4+}$  - 85  $\mu\text{M}$ ,  $\text{Ru}^{3+}$  - 100  $\mu\text{M}$ ,  $\text{Rh}^{3+}$  - 100  $\mu\text{M}$ , details in Methods section.

structural consistency. Although the data shown in Figure 4 demonstrate the formation of well-defined HEA nanoparticles, high-resolution imaging indicates minor local compositional variations. These were analyzed using non-negative matrix factorization (NMF), a dimensionality reduction method applied to hyperspectral EDX data (see Figures S10–S12) [36, 37]. NMF, initially guided by principal component analysis (PCA), decomposes EDX maps into non-negative spectral components and

their corresponding spatial distributions. In one example (Figure S13), NMF revealed two components: one enriched in Au and deficient in Rh–Pd, the other enriched in Rh–Pd and depleted in Au. A similar trend was observed in another sample (Figure S14). However, when analyzing multiple nanoparticles simultaneously, a single component representing all five elements was resolved (Figure S15). At this point it should be noted that incorporating Au into alloys is particularly challenging due

to differences in reduction kinetics and diffusion rates, often resulting in phase segregation when using thermal synthesis approaches. For example, Schneider et al. observed phase separation in Ir–Pt–Cu–Au–Ag thin films due to variations in activation energy barriers for surface diffusion [38]. Despite these challenges, incorporating Au into HEA nanoparticles is of high interest as it can enhance the electrochemical stability of alloy nanoparticles and, in some cases, even improve catalytic activity in electrochemical reactions [39, 40]. Hence, the demonstrated ability to incorporate Au into a single crystallographic phase using our electrodeposition approach represents a significant advancement in HEA nanoparticle synthesis.

Figure 4A–C also illustrates the influence of the electrodeposition potential on grain size. As demonstrated, for Au–Pt–Pd–Rh nanoparticles,  $E_{\text{deposition}} = 0.30 V_{\text{RHE}}$  yields homogeneous  $\sim 20$ – $25$  nm particles. Ir can be uniformly incorporated lowering the electrodeposition potential to  $E_{\text{deposition}} = 0.30 V_{\text{RHE}}$ , yielding Au–Ir–Pt–Pd–Rh without altering the grain size. Incorporating Ru homogeneously was more difficult and did not lead to satisfactory results at  $E_{\text{deposition}} > 0 V_{\text{RHE}}$ . It required lowering the electrodeposition potential to  $E_{\text{deposition}} = -0.05 V_{\text{RHE}}$ , which then resulted in smaller grain sizes ( $\sim 5$ – $6$  nm). This example illustrates the ability to adjust the dimensionality of the composition space of the investigated HEA nanoparticles with a small trade-off between uniform chemical composition and obtained grain size in the electrodeposition-based synthesis for metals that show sluggish deposition behavior in monometallic depositions. We attribute this observation to an increased nucleation rate, which dominates over the surface atom mobility [41]. Conversely, by compromising the incorporation of certain elements such as Ru, growth can be promoted at lower overpotentials, where surface atom mobility outweighs nucleation. For explorative studies of HEA composition spaces, we consider homogeneous compositional mixing more important than uniform grain sizes, as long as the latter is larger than 5 nm where particle size effects are typically less pronounced [42–45]. In addition, the influence

of the electrodeposition potential  $E_{\text{deposition}}$  can partly be counterbalanced by adjusting the pulsing frequency. This is demonstrated based on Au–Ir–Pt–Pd–Rh–Ru nanoparticles (Figure S16A). Notably, higher pulsing frequencies led to increased crystallite sizes and reduced grain agglomeration, whereas lower pulsing frequencies promoted smaller crystallites with greater agglomeration (Figure S16B). At the same time, meso-scale (10–500 nm) EDX quantification revealed that the pulsing frequency had a negligible influence on the Au, Pt, Rh, and Ru content. Only for Ir and Pd, higher pulsing frequencies increased the Ir incorporation while decreasing the Pd content. Hence, the pulsing frequency gives some leverage for optimizing the crystallite size for certain target compositions.

Comprehensive electron microscopy analysis of Au–Ir–Pt–Pd–Rh nanoparticles (Figure 5) further confirms close to homogeneous structural features of the obtained HEA nanoparticles. High-angle annular dark-field (HAADF) imaging (Figure 5A), SAED patterns (Figure 5B), and atomically resolved fast Fourier transform (FFT)s (Figure 5C) all indicate a single FCC phase. For the chosen case, the average lattice parameter ( $3.911 \pm 0.034 \text{ \AA}$ ) closely matches that of pure Pt. 4D-STEM analysis (Figure 5D–G) reveals local crystallographic orientation and strain, as the former is a STEM technique where the diffraction patterns of each probed position are acquired on a pixelated detector [46]. In-plane and out-of-plane maps indicate slight orientation differences between nanodomains. Strain analysis (Figure 5H–J) shows axial and tangential strain, which is indicative of minor local segregation, in a lower-left particle, while the upper-right particle remains single-crystalline. No significant shear strain was observed, suggesting minimal lattice distortion. As the local ordering is observed to be compositional in nature, high-resolution EDX was used to obtain compositional maps. The local composition of the HEA nanoparticle, determined by HR-STEM (Themis-Z), was found to be Au ( $14.3 \pm 0.9 \text{ at\%}$ ), Ir ( $11.2 \pm 0.4 \text{ at\%}$ ), Pt ( $30.3 \pm 2.0 \text{ at\%}$ ), Pd ( $19.4 \pm 4.7 \text{ at\%}$ ), and Rh ( $24.6 \pm 5.2 \text{ at\%}$ ). This closely matches the mesoscale (average)

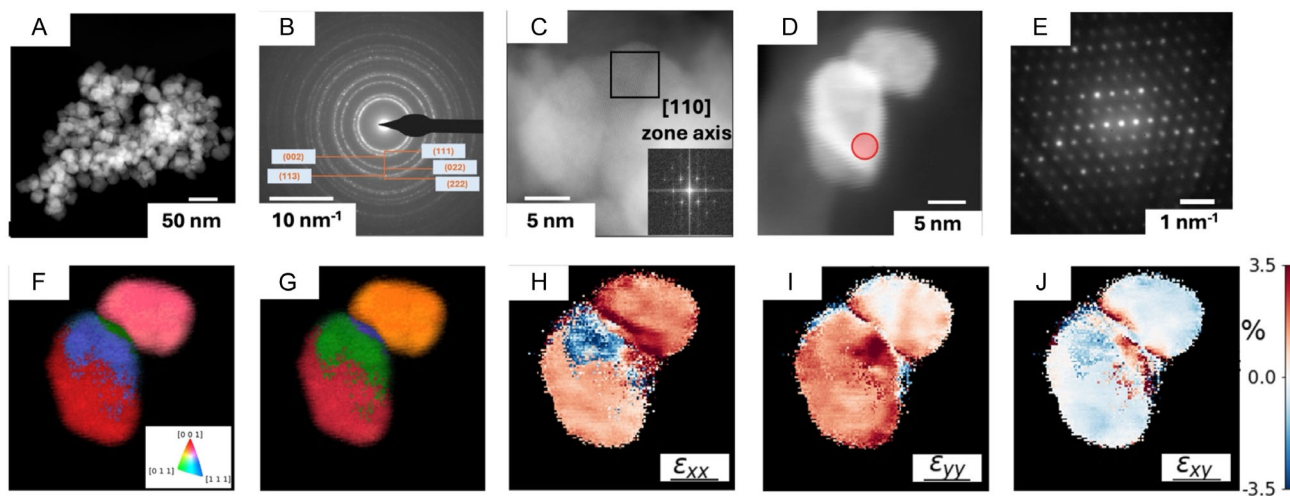


**FIGURE 5** | High-resolution imaging and diffraction data of  $\text{Au}_{14}\text{Ir}_{11}\text{Pt}_{30}\text{Pd}_{20}\text{Rh}_{25}$  nanoparticles. (A) HAADF image of several  $\text{Au}_{14}\text{Ir}_{11}\text{Pt}_{30}\text{Pd}_{20}\text{Rh}_{25}$  nanoparticles, (B) SAED pattern of the nanoparticles in A. (C) Probe-corrected HAADF image, inset displays the fast Fourier transform in [110] zone axis. (D) Virtual annular dark field image of the  $\text{Au}_{14}\text{Ir}_{11}\text{Pt}_{30}\text{Pd}_{20}\text{Rh}_{25}$  crystallites collected by 4D-STEM. (E) Mean diffraction pattern of the red area (in D) near to  $\langle 001 \rangle$  zone axis. (F, G) display the in and out of plane orientational mapping of the nanodomains. (H–J) show the lattice strain mapping with axial strain ( $\epsilon_{xx}$ ) in (H) and tangential strain ( $\epsilon_{yy}$ ) in (I) while shear strain ( $\epsilon_{xy}$ ) in (J). The scale for axial, tangential, and shear strain is common and shown near right of I.

composition of the sample determined via SEM/STEM (Zeiss Gemini), which measured Au ( $16.6 \pm 1.3$  at%), Ir ( $14.0 \pm 1.0$  at%), Pt ( $35.7 \pm 1.0$  at%), Pd ( $12.4 \pm 1.3$  at%), and Rh ( $21.1 \pm 1.4$  at%). Nevertheless, the perceived homogeneity and compositional ordering of the HEA nanoparticles depend on the spatial and spectral resolution of the analysis [47]. This highlights the importance of analyzing the Au–Ir–Pt–Pd–Ru–Rh system across multiple length scales to fully capture compositional variation.

### 3 | A Perspective of HEA Nanoparticle Homogeneity at Different Length Scales

In this section, we discuss the compositional homogeneity of the synthesized samples based on advanced analysis methods. We consider two representative samples, one prepared with equimolar (molar fractions of ca. 0.17) and the other with a nonequimolar bulk electrolyte composition as shown in Figure 6A. For the latter sample, the Au, Ir, and Pt molar fractions are changed from equimolar to 0.04 and 0.12 for Au and Pt, while the Ir molar fraction was increased to 0.29. Figure 6A compares the bulk and diffusion-adjusted electrolyte compositions with the resulting nanoparticle compositions, determined at both the mesoscale (10–500 nm) and nanoscale (0.5–10 nm) by EDX. The mesoscale compositions exhibit narrow distributions in both cases which demonstrates overall sample homogeneity. Furthermore, the mesoscale compositions are close to the diffusion-adjusted electrolyte compositions, demonstrating predictability. By comparison, the nanoscale distribution shows variations in the elemental distribution. Interestingly, the equimolar electrolyte composition leads to broader compositional distribution at the nanoscale than the nonequimolar electrolyte composition, an observation that is also consistent with other nonequimolar electrolyte combinations (see Figures S17–S19). The broader compositional distribution of the sample prepared with equimolar electrolyte composition is characterized by the presence of three different compositional phases. One may suspect that the major reason for the different phases lies in a too-high Au concentration in the bulk electrolyte when using equimolar ratios [48–50]. Computed FE of bimetallic alloys using DFT calculations reveal high positive FE of Au with Ir, Rh, and Ru suggesting a strong tendency for segregation for these metal pairs (Figure S20). Furthermore, Pd–Ru and Pd–Ir exhibit FE > 0.1 eV/atom. To test this hypothesis, we analyzed the variability of all the six elements among various subcompositions within the Au–Ir–Pt–Pd–Rh–Ru compositional space, characterized at mesoscale and nanoscale. For this, the Aitchison variance,  $\text{Var}_{(\text{CLR})}(\mathbf{i})$ , is used as a measure of the homogeneity of each element at the two respective scales (Figure 6B).  $\text{Var}_{(\text{CLR})}(\mathbf{i})$  is the variance of an element after a centered log-ratio (CLR) transformation (for details refer to the Methods section) of the compositional data. The results indicate that all elements exhibit lower variance at the mesoscale (orange boxes) than at the nanoscale (purple boxes). Interestingly, Pd exhibits higher variance than the other elements at the mesoscale. Furthermore, the higher variance at the nanoscale is mainly restricted to Pd and Ru. Computing the inter-variability of the elements using the Aitchison variation ratio,  $T_{i,j}$ , that is,  $\text{Var}[\log \frac{x_i}{x_j}]$  [51] (see Figure 6C), it is seen that the Pd and Ru pairs, that is,  $T_{\text{Pd}}$  and  $T_{\text{Ru}}$ , exhibit the highest variance, not the Au pairs.

Hence, the inhomogeneity is mainly due to these element pairs. We propose that while FE play a role for segregation, the main reason of the observed higher variations can be attributed to the chosen rest potential,  $E_{\text{rest}}$  ( $1.15 V_{\text{RHE}}$ ) as well as the required low deposition potential for Ru. It was found that Pd, in contrast to the other elements, undergoes oxidation at such rest potentials during monometallic depositions, see the potentiodynamic scan in Figure S21. Hence, the observed behavior may be alleviated by either lowering  $E_{\text{rest}}$  or changing to a different Pd precursor which might lead to lower Pd variance at the nanoscale, though this was not further explored in the present study due to restricted access to ultra-high-resolution microscopy.

While Pd and Ru atom pairs may exhibit higher variance for the mentioned reasons, focusing on the other pairs, the results align well with the DFT calculations. Au–Pt, Ir–Rh, and Pt–Rh pairs have a strong mixing tendency in line with the calculated FE. The observed variance across the other atom pairs points towards different degrees of segregation. For example, Au–Ir and Au–Rh exhibit relative high FE as well as relative high variance at the nanoscale. Last but not least, we were able to investigate the HEA homogeneity even within individual nanoparticles at the atomic scale. In Figure 7, an atomically resolved HAADF–STEM image of Au–Ir–Pt–Pd–Rh–Ru nanoparticles prepared from equimolar bulk electrolyte composition is shown together with EDX maps of all the elements. Figure 8 shows the respective NMF decompositions of the hyperspectral dataset of the crystalline domains.

Based on the analysis in Figure 8, the nanoparticle composition can be divided into three components (factors), see also the scree plot in Figure S22. The elemental composition of the three factors was determined using the Cliff–Lorimer method. The first component contains all six elements above 12.5 at%, that is, it is close to an equimolar composition ( $\sim 16.7$  at%), and exhibits a maximum explained variance ratio of  $\sim 0.60$ . The variance ratio carries the weight of the respective component in the total variance of the data. Therefore, it can be used as a quantification of the components to get a quantifiable estimate of spectral factors in Figure 8. Hence, even on an atomic scale the individual nanoparticle exhibits a high degree of mixing. However, the second component indicates the presence of an Au-enriched segregated phase which has explained variance ratio of  $\sim 0.23$ . Herein term “enrichment” of an element is defined as a deviation from the average composition of the individual particle. Au–Pt enrichment is consistent with the observations made from the analysis at nanoscale in Figure 6C. Furthermore, a third component was found with a variance ratio of  $\sim 0.17$ , which is enriched in Au, Pd, Pt, and Rh. Thus, NMF decomposition provides evidence of element mixing with certain extent of ordering in terms of segregation by identifying patterns in compositional data.

In summary, this study presents a medium-throughput approach for synthesizing HEA nanoparticles via electrodeposition in aqueous media. The method is both rapid and efficient, and it is compatible with various conductive carbon substrates. A pulsed electrodeposition protocol facilitates the formation of nonagglomerated, single-phase HEA nanoparticles with sizes ranging from 5 to 30 nm. By tuning the electrolyte composition and controlling diffusion parameters, the average particle composition can be predicted with high accuracy.

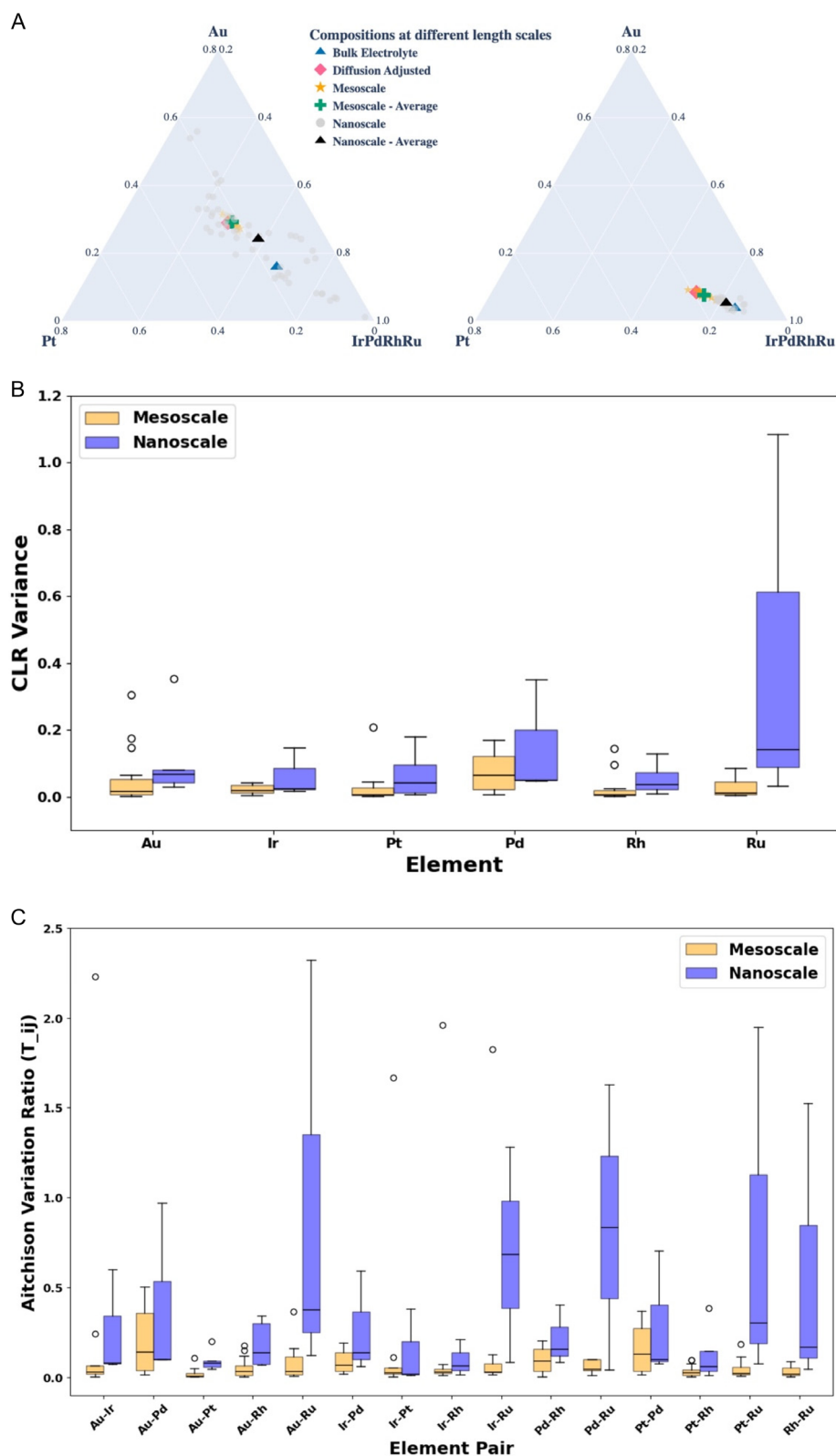


**FIGURE 6** | (A) Illustrates an equimolar (left) and nonequimolar (right) bulk electrolyte-based samples of Au–Ir–Pt–Pd–Rh–Ru. Nonequimolar bulk electrolyte composition is Au (0.038), Ir (0.291), Pt (0.116), Pd (0.165), Rh (0.194), and Ru (0.194) in molar fractions. It shows compositions observed at different length scales in simplex space. (B) Shows CLR variance, that is,  $\text{Var}_{(\text{CLR})}(i)$ , of all the six elements in mesoscale and nanoscale compositional dataset. Small white circles shown are the outliers out of whiskers. (C) Shows box-plot of Aitchison variation ratio of different element pairs computed using mesoscale and nanoscale compositional data of various samples used in the current study. Twenty-six samples synthesized on GC were analyzed for mesoscale compositions (1110 spectra), while 5 of them were chosen for nanoscale compositions (340 spectra).



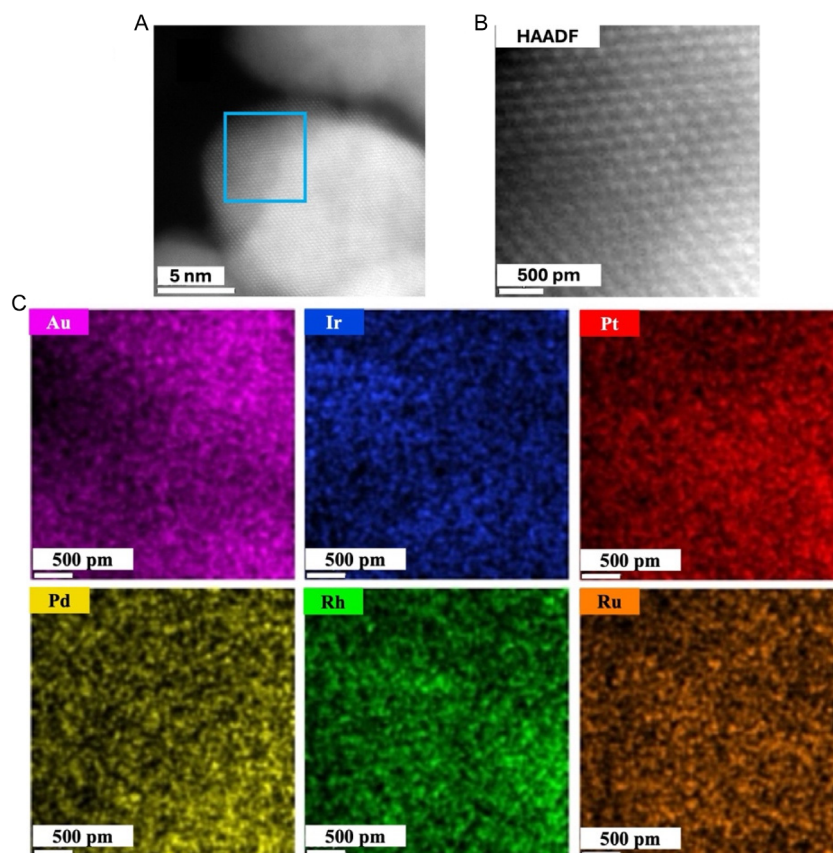


**FIGURE 7** | (A) Atomically resolved HAADF-STEM image of Au-Ir-Pt-Pd-Rh-Ru nanodomains. (B) Depicts the zoomed-in image of the blue square which was selected for the spectral mapping. (C) Shows the corresponding EDX maps of all the six elements.

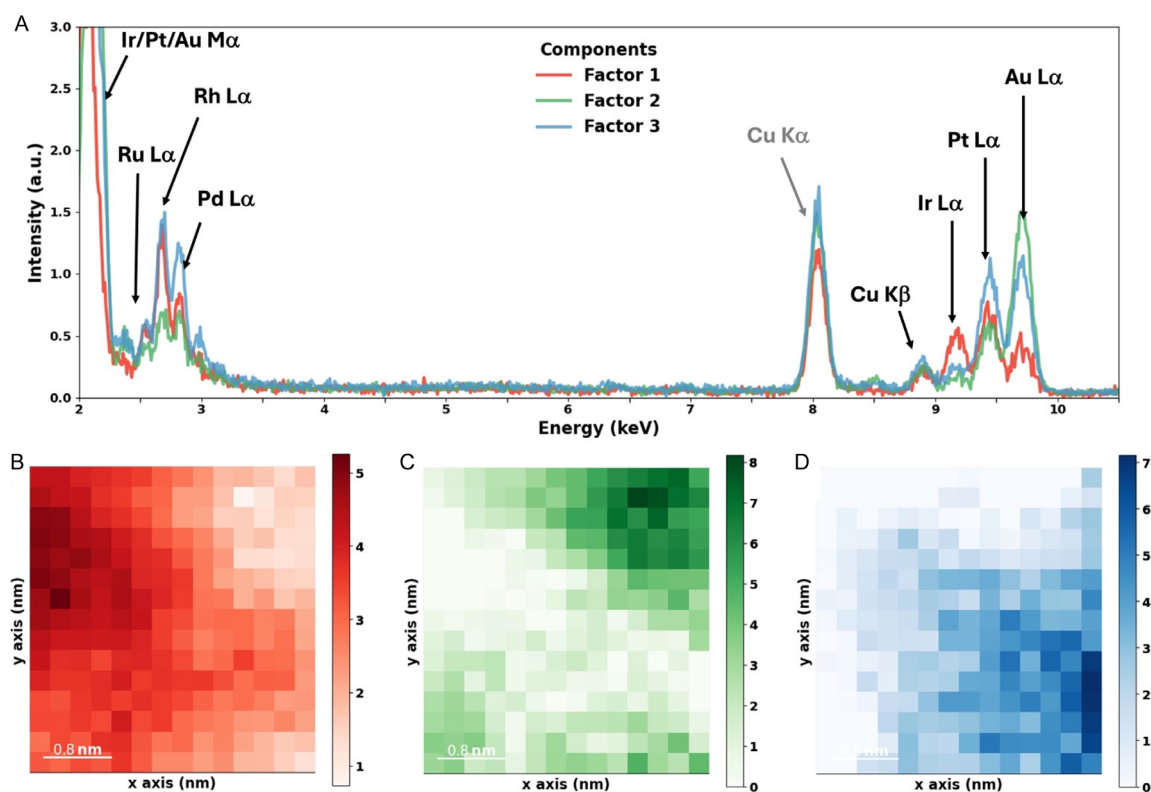


**FIGURE 8** | (A) Non-negative matrix factorization of a hyperspectral dataset collected using probe corrected HAADF-STEM imaging and EDX mapping of a Au-Ir-Pt-Pd-Rh-Ru nanoparticle (on Copper grid) domain synthesized from equimolar bulk electrolyte concentration. Spectral factors are shown at the top and the respective spatial loadings in (B) Red, (C) Green, and (D) Blue for 1<sup>st</sup>, 2<sup>nd</sup>, and 3<sup>rd</sup> component, respectively. Spatial re-binning of  $7 \times 7$  was performed to increase the signal-to-noise ratio before the NMF decomposition.

Homogeneity in alloy nanoparticles is typically assessed through EDX mapping, as illustrated in Figure 2. In such analysis, the HEA nanoparticles display a high degree of compositional uniformity. Our advanced microscopy techniques reveal that this observed homogeneity is scale dependent. While the nanoparticles appear highly homogeneous at the mesoscale (10–500 nm), slight variations in composition become evident when analyzing statistics at the nanoscale (0.5–10 nm) and even at the atomic scale. The observed ordering and segregation at the nanoscale can be partly attributed to constraints such as sluggish electrodeposition kinetics of specific metals as well as their oxidation at the rest potential. Additionally, the FE of bimetallic atom pairs influence the compositional uniformity at the nanoscale. These insights not only advance our understanding of compositional control in HEA nanoparticles but also open up new avenues for tailoring their structure and functionality for future applications in catalysis, energy storage, and beyond.

## Author Contributions

**Divyansh Gautam:** conceptualization (lead), data curation (lead), formal analysis (lead), investigation (lead), writing – original draft (lead), writing – review and editing (equal). **Gustav K. H. Wiberg:** conceptualization (lead), data curation (supporting), formal analysis (supporting), supervision (supporting), writing review and editing (supporting). **Jonathan Quinson:** formal analysis (supporting), investigation (supporting), writing – original draft (supporting), writing review and editing (supporting). **Di Wang:** formal analysis (supporting), investigation (supporting), writing review and editing (supporting). **Christian M. Clausen:** formal analysis (supporting), investigation (supporting), writing review and editing (supporting). **Rasmus Rohde:** formal analysis (supporting), investigation (supporting), writing review and editing (supporting). **Rebekka Klemmt:** formal analysis (supporting), investigation (supporting), writing review and editing (supporting). **Jan Rossmeisl:** formal analysis (supporting), resources (supporting), supervision (supporting), writing review and editing (supporting), writing review and editing (supporting). **Espen Drath Bøjesen:** formal analysis (supporting), validation (supporting), formal analysis (supporting), resources (supporting), supervision (supporting), writing review and editing (supporting). **Matthias Arenz:** conceptualization (lead), formal analysis (supporting), funding acquisition (lead), project administration (lead), resources (lead), supervision (lead), writing – original draft (equal), writing – review and editing (equal).

## Acknowledgments

M.A. and J.R. acknowledge financial the support from the European Union under the ERC Synergy grant DEMI, GA no. 101118768 as well as support from the Danish National Research Foundation Center for High Entropy Alloy Catalysis (DNRF 149). This work was partly carried out with the support of the Karlsruhe Nano Micro Facility (KNMF, <https://www.knmf.kit.edu>), a Helmholtz Research Infrastructure at Karlsruhe Institute of Technology (KIT, <https://www.kit.edu>). Beamline ID-31, proposal number IH-MA-436, at the European Synchrotron Research Facility in Grenoble, France, is acknowledged for the collection of the total scattering from the GDL samples. J.Q. is thankful to the Aarhus University Research Foundation, grant number AUFF-E-2022-9-40. R.R. acknowledges funding from Innovation Fund Denmark for the HyProFuel project (File No. 1062-00026A). R.K. and E.D.B. acknowledge funding from the CENSEMAT (DNRF189) and Aarhus University Centre for Integrated Materials Research. M.A. acknowledges financial support from the Swiss National Science Foundation, grant no. 10001494.

Open access publishing facilitated by Universitat Bern, as part of the Wiley - Universitat Bern agreement via the Consortium of Swiss Academic Libraries.

## Funding

This study was supported by H2020 European Research Council (Grant 101118768), Danmarks Grundforskningsfond (Grant DNRF 149), Naturvidenskab og Teknologi, Aarhus Universitet (Grant AUFF-E-2022-9-40), Innovationsfonden (Grant 1062-00026A), Danmarks Grundforskningsfond (Grant DNRF189), and Schweizerischer Nationalfonds zur Förderung der Wissenschaftlichen Forschung (Grant 10001494).

## Conflicts of Interest

The authors declare no conflicts of interest.

## Use of AI

The authors declare the use of Artificial Intelligence (AI) in copy editing, that is, the authors used programs such as ChatGPT for improving their texts in terms of readability and style as well as to ensure that the manuscript is free of errors in grammar, spelling, punctuation, and tone. The authors used ChatGPT in formulating and editing Python scripts for plotting the figures, however, no generative editorial work and autonomous content creation were used.

## Data Availability Statement

All the raw data, scripts, and processed data are available under <https://doi.org/10.5281/zenodo.17506187>.

## References

1. J. W. Yeh, S. K. Chen, S. J. Lin, et al., “Nanostructured High-Entropy Alloys with Multiple Principal Elements: Novel Alloy Design Concepts and Outcomes,” *Advanced Engineering Materials* 6 (2004): 299–303.
2. B. Cantor, “Multicomponent and High Entropy Alloys,” *Entropy* 16 (2014): 4749–4768.
3. E. P. George, D. Raabe, and R. O. Ritchie, “High-Entropy Alloys,” *Nature Reviews Materials* 4 (2019): 515–534, Preprint at <https://doi.org/10.1038/s41578-019-0121-4>
4. Y. F. Ye, Q. Wang, J. Lu, C. T. Liu, and Y. Yang, “High-Entropy Alloy: Challenges and Prospects,” *Materials Today* 19 (2016): 349–362, Preprint at <https://doi.org/10.1016/j.mattod.2015.11.026>.
5. B. Gludovatz, A. Hohenwarter, D. Catoor, E. H. Chang, E. P. George, and R. O. Ritchie, “A Fracture-Resistant High-Entropy Alloy for Cryogenic Applications,” *Science* 345 (2014): 1153–1158.
6. Q. Ding, Y. Zhang, X. Chen, et al., “Tuning Element Distribution, Structure and Properties by Composition in High-Entropy Alloys,” *Nature* 574 (2019): 223–227.
7. T. A. A. Batchelor, J. K. Pedersen, S. H. Winther, I. E. Castelli, K. W. Jacobsen, and J. Rossmeisl, “High-Entropy Alloys as a Discovery Platform for Electrocatalysis,” *Joule* 3 (2019): 834–845.
8. A. Ludwig, “Discovery of New Materials Using Combinatorial Synthesis and High-Throughput Characterization of Thin-Film Materials Libraries Combined with Computational Methods,” *Npj Computational Materials* 5 (2019): 1–7.
9. T. Löffler, A. Ludwig, J. Rossmeisl, and W. Schuhmann, “What Makes High-Entropy Alloys Exceptional Electrocatalysts?,” *Angewandte Chemie International Edition* 60 (2021): 26894–26903, Preprint at <https://doi.org/10.1002/anie.202109212>.
10. J. K. Pedersen, C. M. Clausen, O. A. Krysiak, et al., “Bayesian Optimization of High-Entropy Alloy Compositions for Electrocatalytic Oxygen Reduction,” *Angewandte Chemie International Edition* 60 (2021): 24144–24152.
11. V. A. Mints, J. K. Pedersen, A. Bagger, et al., “Exploring the Composition Space of High-Entropy Alloy Nanoparticles for the

- Electrocatalytic  $\text{H}_2/\text{CO}$  Oxidation with Bayesian Optimization,” *ACS Catalysis* 12 (2022): 11263–11271.
12. V. A. Mints, K. L. Svane, J. Rossmeisl, and M. Arenz, “Exploring the High-Entropy Oxide Composition Space: Insights through Comparing Experimental with Theoretical Models for the Oxygen Evolution Reaction,” *ACS Catalysis* 14 (2024): 6936–6944.
  13. R. K. Pittkowski, C. M. Clausen, Q. Chen, et al., “The More the Better: On the Formation of Single-Phase High Entropy Alloy Nanoparticles as Catalysts for the Oxygen Reduction Reaction,” *EES Catalysis* 1 (2023): 950–960.
  14. W. Xu, E. Diesen, T. He, K. Reuter, and J. T. Margraf, “Discovering High Entropy Alloy Electrocatalysts in Vast Composition Spaces with Multiobjective Optimization,” *Journal of the American Chemical Society* 146 (2024): 7698–7707.
  15. T. A. A. Batchelor, T. Löffler, B. Xiao, et al., “Complex-Solid-Solution Electrocatalyst Discovery by Computational Prediction and High-Throughput Experimentation\*\*,” *Angewandte Chemie International Edition* 60 (2021): 6932–6937.
  16. L. Banko, O. A. Krysiak, J. K. Pedersen, et al., “Unravelling Composition–Activity–Stability Trends in High Entropy Alloy Electrocatalysts by Using a Data-Guided Combinatorial Synthesis Strategy and Computational Modeling,” *Advanced Energy Materials* 12 (2022): 2103312.
  17. T. X. Nguyen, Y.-H. Su, J. Hattrick-Simpers, et al., “Exploring the First High-Entropy Thin Film Libraries: Composition Spread-Controlled Crystalline Structure,” *ACS Combinatorial Science* 22 (2020): 858–866.
  18. Y. Yao, Q. Dong, A. Brozena, et al., “High-Entropy Nanoparticles: Synthesis-Structure-Property Relationships and Data-Driven Discovery,” *Science* 376 (2022): eabn3103.
  19. V. A. Mints, J. K. Pedersen, G. K. H. Wiberg, J. Rossmeisl, and M. Arenz, “Backward Elimination: A Strategy for High-Entropy Alloy Catalyst Discovery,” *ChemRxiv Preprint* 2022, <https://doi.org/10.26434/chemrxiv-2022-78s83>.
  20. X. Chen, Q. Wang, Z. Cheng, et al., “Direct Observation of Chemical Short-Range Order in a Medium-Entropy Alloy,” *Nature* 592 (2021): 712–716.
  21. S. Chen, Z. H. Aitken, S. Pattamatta, et al., “Simultaneously Enhancing the Ultimate Strength and Ductility of High-Entropy Alloys via Short-Range Ordering,” *Nature Communications* 12 (2021): 1–11.
  22. Z. Huang, T. Li, B. Li, et al., “Tailoring Local Chemical Ordering via Elemental Tuning in High-Entropy Alloys,” *Journal of the American Chemical Society* 146 (2024): 2167–2173.
  23. Z. W. Lu, B. M. Klein, and A. Zunger, “Ordering Tendencies in Pd-Pt, Rh-Pt, and Ag-Au Alloys,” *Journal of Phase Equilibria* 16 (1995): 36–45.
  24. Y. Yao, Z. Huang, P. Xie, et al., “Carbothermal Shock Synthesis of High-Entropy-Alloy Nanoparticles,” *Science* (1979) 359 (2018): 1489–1494.
  25. M. Bondesgaard, N. L. N. Broge, A. Mamakhel, M. Bremholm, and B. B. Iversen, “General Solvothermal Synthesis Method for Complete Solubility Range Bimetallic and High-Entropy Alloy Nanocatalysts,” *Advanced Functional Materials* 29 (2019): 1–9.
  26. H. Qiao, M. T. Saray, X. Wang, et al., “Scalable Synthesis of High Entropy Alloy Nanoparticles by Microwave Heating,” *ACS Nano* 15 (2021): 14928–14937.
  27. D. Wu, K. Kusada, Y. Nanba, et al., “Noble-Metal High-Entropy-Alloy Nanoparticles: Atomic-Level Insight into the Electronic Structure,” *Journal of the American Chemical Society* 144 (2022): 3365–3369.
  28. T. G. Ritter, S. Pappu, and R. Shahbazian-Yassar, “Scalable Synthesis Methods for High-Entropy Nanoparticles,” *Advanced Energy and Sustainability Research* 5 (2024): 2300297.
  29. M. L. Personick, A. A. Jallow, G. C. Halford, and L. A. Baker, “Nanomaterials Synthesis Discovery via Parallel Electrochemical Deposition,” *Chemistry of Materials* 36 (2024): 3034–3041.
  30. A. L. Wang, H. C. Wan, H. Xu, Y. X. Tong, and G. R. Li, “Quinary PdNiCoCuFe Alloy Nanotube Arrays as Efficient Electrocatalysts for Methanol Oxidation,” *Electrochimica Acta* 127 (2014): 448–453.
  31. Z. Shojaei, G. R. Khayati, and E. Darezereshki, “Review of Electrodeposition Methods for the Preparation of High-Entropy Alloys,” *International Journal of Minerals, Metallurgy and Materials* 29 (2022): 1683–1696.
  32. Y. J. Deng, G. K. H. Wiberg, A. Zana, S. G. Sun, and M. Arenz, “Tetrahexahedral Pt Nanoparticles: Comparing the Oxygen Reduction Reaction under Transient vs Steady-State Conditions,” *ACS Catalysis* 7 (2017): 1–6.
  33. M. K. Plenge, J. K. Pedersen, V. A. Mints, M. Arenz, and J. Rossmeisl, “Following Paths of Maximum Catalytic Activity in the Composition Space of High-Entropy Alloys,” *Advanced Energy Materials* 13 (2023): 2202962.
  34. A. Saksena, D. Bogdanovski, H. Sahasrabudhe, D. Music, and J. M. Schneider, “Kinetically Limited Phase Formation of Pt-Ir Based Compositionally Complex Thin Films,” *Materials* 13, (2020): 2298.
  35. M. Sankar, Q. He, R. V. Engel, et al., “Role of the Support in Gold-Containing Nanoparticles as Heterogeneous Catalysts,” *Chemical Reviews* 120 (2020): 3890, Preprint at <https://doi.org/10.1021/acs.chemrev.9b00662>.
  36. H. Chen, D. T. L. Alexander, and C. Hébert, “Leveraging Machine Learning for Advanced Nanoscale X-ray Analysis: Unmixing Multicomponent Signals and Enhancing Chemical Quantification,” *Nano Letters* 24 (2024): 10177–10185.
  37. H. Chen, F. Nabiei, J. Badro, D. T. L. Alexander, and C. Hébert, “Non-Negative Matrix Factorization-Aided Phase Unmixing and Trace Element Quantification of STEM-EDXS Data,” *Ultramicroscopy* 263 (2024): 113981.
  38. A. Saksena, D. Bogdanovski, H. Sahasrabudhe, D. Music, and J. M. Schneider, “Kinetically Limited Phase Formation of Pt-Ir Based Compositionally Complex Thin Films,” *Materials* 13 (2020): 1–11.
  39. M. Sankar, Q. He, R. V. Engel, et al., “Role of the Support in Gold-Containing Nanoparticles as Heterogeneous Catalysts,” *Chemical Reviews* 120 (2020): 3890–3938.
  40. P. P. Lopes, D. Li, H. Lv, et al., “Eliminating Dissolution of Platinum-Based Electrocatalysts at the Atomic Scale,” *Nature Materials* 19 (2020): 1207–1214.
  41. Q. Zhang, J. Wan, J. Shangguan, S. Betzler, and H. Zheng, “Influence of Sub-Zero Temperature On Nucleation and Growth of Copper Nanoparticles in Electrochemical Reactions,” *iScience* 24 (2021): 103289.
  42. M. Nesselberger, S. Ashton, J. C. Meier, I. Katsounaros, K. J. J. Mayrhofer, and M. Arenz, “The Particle Size Effect on the Oxygen Reduction Reaction Activity of Pt Catalysts: Influence of Electrolyte and Relation to Single Crystal Models,” *Journal of the American Chemical Society* 133 (2011): 17428–17433.
  43. M. Inaba, A. Zana, J. Quinson, et al., “The Oxygen Reduction Reaction On Pt: Why Particle Size and Interparticle Distance Matter,” *ACS Catalysis* 11 (2021): 7144–7153.
  44. K. J. J. Mayrhofer, B. B. Blizanac, M. Arenz, V. R. Stamenkovic, P. N. Ross, and N. M. Markovic, “The Impact of Geometric and Surface Electronic Properties of Pt-Catalysts On the Particle Size Effect in Electrocatalysis,” *Journal of Physical Chemistry B* 109 (2005): 14433.
  45. M. Arenz, K. J. J. Mayrhofer, V. Stamenkovic, et al., “The Effect of the Particle Size On the Kinetics of CO Electrooxidation On High Surface Area Pt Catalysts,” *Journal of the American Chemical Society* 127 (2005): 6819.



46. C. Ophus, S. E. Zeltmann, A. Bruefach, et al., "Automated Crystal Orientation Mapping in py4DSTEM Using Sparse Correlation Matching," *Microscopy and Microanalysis* 28 (2022): 390–403.
47. Y. Han, H. Chen, Y. Sun, et al., "Ubiquitous Short-Range Order in Multi-Principal Element Alloys," *Nature Communications* 15 (2024): 1–13.
48. G. Breyton, H. Amara, J. Nelayah, et al., "Atomic-Scale Surface Segregation in Copper-Gold Nanoparticles," *Physical Review Letters* 130 (2023): 236201.
49. L. Piccolo, Z. Y. Li, I. Demiroglu, et al., "Understanding and Controlling the Structure and Segregation Behaviour of AuRh Nanocatalysts," *Scientific Reports* 6 (2016): 1–8.
50. Q. Zhang, K. Kusada, D. Wu, et al., "Solid-Solution Alloy Nanoparticles of a Combination of Immiscible Au and Ru with a Large Gap of Reduction Potential and Their Enhanced Oxygen Evolution Reaction Performance," *Chemical Science* 10 (2019): 5133–5137.
51. A. R. Bennett, J. Lundström, S. Chatterjee, M. Thaysen-Andersen, and D. Bojar, "Compositional Data Analysis Enables Statistical Rigor in Comparative Glycomics," *Nature Communications* 16 (2025): 1–15.

## Supporting Information

Additional supporting information can be found online in the Supporting Information Section. Additional characterization, information on the various compositions used in the manuscript, along with supporting data of monometallic depositions. **Supporting Fig. S1:** Electrochemical cell used for electrodeposition. **Supporting Fig. S2:** SEM micrographs of different samples prepared at five potential holds to get an overview of kinetic limitations of Ir-Pt-Pd-Ru-Rh system for designing pulse voltammetry protocol. **Supporting Fig. S3:** NMF factorization of the hyperspectral dataset collected from Ir-Pt-Pd-Rh-Ru NPs, justifying mixing of all the five elements. A) shows the scree plot after principal component analysis. B-C shows the spatial loadings of the respective spectral factors. **Supporting Fig. S4:** A-B) aberration corrected HR-TEM micrographs of Ir-Pt-Pd-Rh-Ru nanoparticles which shows defect rich nanodomains marked by orange arrows. C) shows an HAADF-STEM image of a cluster of nanoparticles while D) shows the SAED pattern of the same area in TEM mode. **Supporting Fig. S5:** Watershed algorithm to perform segmentation and estimating particle size. A) grey scale image taken from Inlens detector of Gemini SEM 450. B) image showing segmented particles after Otsu' thresholding. C) Distribution of particle size as per the segmented image. **Supporting Fig. S6:** A) Current versus potential plotted from potentiostatic protocol of Gold electrodeposition on Gold surface (pH = 2.5, solution resistance ( $R_s$ ) = 6–9  $\Omega$ ). B) shows current versus potential plotted from potentiostatic protocol of Iridium electrodeposition on Platinum surface (pH = 4.0,  $R_s$  = 7–9  $\Omega$ ). C) shows current versus potential plotted from potentiostatic protocol of Platinum electrodeposition on Platinum surface (pH = 3.0,  $R_s$  = 3–4  $\Omega$ ). D) shows current versus potential plotted from potentiostatic protocol of Palladium electrodeposition on Palladium surface (pH = 2.5,  $R_s$  = 1–2  $\Omega$ ). E) shows current versus potential plotted from potentiostatic protocol of Rhodium electrodeposition on Rhodium surface (pH = 2.6,  $R_s$  = 5–7  $\Omega$ ). F) shows current versus potential plotted from potentiostatic protocol of Ruthenium electrodeposition on Platinum surface (pH = 4.3,  $R_s$  = 6–7  $\Omega$ ). **Supporting Fig. S7:** A) Steady state current (0.05  $V_{RHE}$  or -0.3  $V_{Ag/AgCl}$ ) vs rotation rate of Gold electrodeposition on Gold surface. B) Steady state current (0.05  $V_{RHE}$  or -0.3  $V_{Ag/AgCl}$ ) vs rotation rate of Iridium electrodeposition on Platinum surface. C) Steady state current (0.05  $V_{RHE}$  or -0.3  $V_{Ag/AgCl}$ ) vs rotation rate of Platinum electrodeposition on Platinum surface. D) Steady state current (0.05  $V_{RHE}$  or -0.3  $V_{Ag/AgCl}$ ) vs rotation rate of Palladium electrodeposition on Palladium surface. E) Steady state current (0.05  $V_{RHE}$  or -0.3  $V_{Ag/AgCl}$ ) vs rotation rate of Rhodium electrodeposition on Rhodium surface. F) Steady state current (0.05  $V_{RHE}$  or -0.3  $V_{Ag/AgCl}$ ) vs rotation rate of Ruthenium electrodeposition on Platinum

surface. **Supporting Fig. S8:** Compositional evolution of different elements with respect to the duration of synthesis on Ketjen Black. The samples were prepared on KB with the synthesis methodology discussed in methods. 1 min synthesis has 10 pulses, 5 min has 50 pulses, and 20 min consists of 200 pulses. A) and B) displays the local EDX composition from NPs of Au-Ir-Pt-Pd-Rh-Ru and Ir-Pt-Pd-Rh-Ru system respectively. Concentration of metal cations in electrolyte were as follows:  $Au^{3+}$  - 5  $\mu M$ ,  $Ir^{4+}$  - 15  $\mu M$ ,  $Pt^{4+}$  - 8.5  $\mu M$ ,  $Pd^{4+}$  - 8.5  $\mu M$ ,  $Ru^{3+}$  - 8.5  $\mu M$ ,  $Rh^{3+}$  - 10  $\mu M$  for the synthesis on KB. In B) the same bulk electrolyte composition was used while not having Au. **Supporting Fig. S9:** A, B, C) shows three simplex plots representing the Au-Ir-Pt-Pd-Rh-Ru compositional vector space while plotting global EDX (average composition), diffusion rate corrected and bulk electrolyte compositions. Black continuous lines join global EDX to diffusion adjusted compositions and grey dashed lines connect global EDX with bulk electrolyte compositions. D) shows the euclidean distances in the centered log-ratio transformed (CLR) space of mesoscale average compositions, bulk electrolyte and diffusion adjusted compositions. **Supporting Fig. S10:** PCA scree plots and the NMF decomposition of hyperspectral dataset of Au-Pt-Pd-Rh (binned by a factor of 10). EDX composition of the sample were determined as Au-Pt-Pd-Rh; Au ( $19.5 \pm 2.6$ ), Pt ( $37.0 \pm 2.6$ ), Pd ( $11.8 \pm 0.7$ ), Rh ( $29.7 \pm 3.6$ ). Here loading 0 shows the background spatial signal which is evident from its corresponding factor 0. Loading 1 shows the distribution of Au, Pt, Pd and Rh in a single component, which can be validated from the respective factor 1. There is an observable peak of Ir in the spectra, however it was being neglected from the quantification point of view in Velox. Therefore, Ir is also not shown in elemental maps in Figure 4, as the distribution of Ir can lead to misinterpretation of its significant presence. **Supporting Fig. S11:** PCA scree plots and the NMF decomposition of hyperspectral dataset of Au-Ir-Pt-Pd-Rh (binned by a factor of 10). Nanoscale EDX composition of the sample were determined as Au-Ir-Pt-Pd-Rh - Au ( $14.3 \pm 3.0$ ), Ir ( $11.2 \pm 1.0$ ), Pt ( $30.3 \pm 2.0$ ), Pd ( $19.4 \pm 1.3$ ), Rh ( $24.6 \pm 2.1$ ). Here loading 0 shows the background spatial signal which is evident from its corresponding factor 0. Loading 1 shows the distribution of Au, Ir, Pt, Pd and Rh in a single component, which can be validated from the respective factor 1. **Supporting Fig. S12:** PCA scree plots and the NMF decomposition of hyperspectral dataset of Au-Ir-Pt-Pd-Rh-Ru (binned by a factor of 6). Nanoscale EDX composition of the sample were determined as Au-Ir-Pt-Pd-Rh-Ru - Au ( $5.2 \pm 0.1$ ), Ir ( $21.0 \pm 3.2$ ), Pt ( $13.2 \pm 1.6$ ), Pd ( $22.0 \pm 4.9$ ), Rh ( $21.4 \pm 1.9$ ) and Ru ( $17.1 \pm 2.6$ ). Here loading 0 shows the background spatial signal which is evident from its corresponding factor 0. Loading 1 shows the distribution of Au, Ir, Pt, Pd, Rh and Ru in a single component, which can be validated from the respective factor 1. **Supporting Fig. S13:** A) Scree plot using the hyperspectral dataset, re-binned by a factor of  $3 \times 3 \times 1$ , i.e., spectral data is used as it is and only the spatial intensities of the pixels are binned. Here 3 components explaining most of the variance were further used for NMF decomposition. B), C) and D) shows the loadings of the factors shown in E), F) and G) respectively. Segregation of Au and Pd is found in factor 1 which spatially is shown in loading 1. Moreover, factor 2 shows the relative decrement in Au and Pd intensities with respect to factor 1. Loading 1 shows the distribution of Au and Pd deficient region. **Supporting Fig. S14:** Example of the local compositional order found in an Au-Ir-Pt-Pd-Rh NP. A) represents the HAADF image of Au-Ir-Pt-Pd-Rh system and the corresponding EDX maps of incorporated elements. B) shows the PCA scree plot of the hyperspectral dataset binned by a factor of  $10 \times 10 \times 1$ . C), D) and E) shows the different loadings corresponding to F), G) and H) factors respectively. Factor 2 has relatively high ratio of Pd and Rh than Factor 1 showing an extent of segregation within the NP between Pd, Rh and rest of the elements. **Supporting Fig. S15:** A) EDX maps of multiple Au-Ir-Pt-Pd-Rh NPs. B) shows the PCA scree plot (without binning). C) and D) shows the NMF loadings of the respective factors shown in E) and F). Here in case of multiple NPs, the segregation observed in Supporting Fig. 12–13 is not observable and Au, Ir, Pt, Pd and Rh seem to be well mixed. **Supporting Fig. S16:** A) shows the diffusion adjusted composition and the mesoscale average EDX compositions (Right y-axis; scatter points plot) of four different samples of Au-Ir-Pt-Pd-Rh-Ru NPs synthesized at four different pulsing frequencies (100, 20, 2 and 0.5 Hz) on glassy carbon. Black dashed line shows the equimolar bulk electrolyte composition. B) shows the TEM micrographs of the



samples prepared at different pulsing frequency with equimolar ratio of the precursors in the electrolyte. Synthesis procedure, equimolar ratio of all the six elements was used with total concentration of precursors being 500  $\mu\text{M}$  in the electrolyte. Potentials used were  $E_{\text{insertion}} = 1.2 \text{ V}_{\text{RHE}}$  (for 2 minutes),  $E_{\text{nucleation}} = -0.15 \text{ V}_{\text{RHE}}$  (for 2 seconds),  $E_{\text{deposition}} = -0.10 \text{ V}_{\text{RHE}}$  and  $E_{\text{rest}} = 1.15 \text{ V}_{\text{RHE}}$  with  $Rt = 1.0$  for 90 sec. **Supporting Fig. S17:** Shows the three compositionally distinctive phases of Au-Ir-Pt-Pd-Rh-Ru NPs made with equimolar bulk electrolyte concentration where A) is Au enriched having Au ( $27.8 \pm 9.8$ ), Ir ( $7.9 \pm 3.0$ ), Pt ( $21.0 \pm 3.5$ ), Pd ( $12.3 \pm 3.8$ ), Rh ( $20.5 \pm 3.4$ ) and Ru ( $10.2 \pm 5.2$ ). B) is Pd enriched with average compositions Au ( $7.3 \pm 0.9$ ), Ir ( $7.2 \pm 0.9$ ), Pt ( $8.5 \pm 1.6$ ), Pd ( $45.3 \pm 4.7$ ), Rh ( $17.3 \pm 1.7$ ) and Ru ( $14.2 \pm 1.0$ ). C) shows Ru enriched 1-2 nm clusters with an average composition of Au ( $1.2 \pm 0.1$ ), Ir ( $5.7 \pm 0.3$ ), Pt ( $1.8 \pm 0.0$ ), Pd ( $0.4 \pm 0.07$ ), Rh ( $15.8 \pm 0.6$ ) and Ru ( $74.7 \pm 0.9$ ). **Supporting Fig. S18:** Single compositional Ir enriched phase of Au-Ir-Pt-Pd-Rh-Ru NPs made with non-equimolar bulk electrolyte concentration. There average composition (nanoscale EDX) is Au ( $5.2 \pm 0.1$ ), Ir ( $21.0 \pm 3.2$ ), Pt ( $13.2 \pm 1.6$ ), Pd ( $22.0 \pm 4.9$ ), Rh ( $21.5 \pm 1.9$ ) and Ru ( $17.1 \pm 2.6$ ). Non-equimolar bulk electrolyte composition is Au (0.038), Ir (0.291), Pt (0.116), Pd (0.165), Rh (0.194) and Ru (0.194) in molar fractions. **Supporting Fig. S19:** Simplex plots of equimolar (A) and non-equimolar (B) bulk electrolyte composition-based samples shown in Figure S17 and Figure S18 respectively. **Supporting Fig. S20:** Formation energies in eV/atom computed for binary alloys based on face-centered cubic (FCC) bulk cells containing 4 atoms of each element in a Rocksalt-type structure. **Supporting Fig. S21:** A) Cyclic voltammograms (CVs) of Gold electrodeposition on Gold surface (pH = 2.5, solution resistance (Rs) = 6-9  $\Omega$ ). B) CVs of Iridium electrodeposition on Platinum surface (pH = 4.0, Rs = 7-9  $\Omega$ ). C) shows CVs of Platinum electrodeposition on Platinum surface (pH = 3.0, Rs = 3-4  $\Omega$ ). D) CVs of Palladium electrodeposition on Palladium surface (pH = 2.5, Rs = 1-2  $\Omega$ ). E) CVs of Rhodium electrodeposition on Rhodium surface (pH = 2.6, Rs = 5-7  $\Omega$ ). F) CVs of Ruthenium electrodeposition on Platinum surface (pH=4.3, Rs = 6-7  $\Omega$ ). **Supporting Fig. S22:** A) Scree plot of the principal component analysis after (7x7x1) spatial binning of the hyperspectral dataset. B) Variance ratio (ratio of the proportion of variance shown by that component to the total variance shown by the three components) of the selected first three components. C) EDX quantification of the three spectral factors corresponding to the three components after the NMF decomposition. The quantification performed here is using the Cliff Lorimer method using the manufacturer provided k-factors (All L lines were chosen) of all the six elements. Python package Hyperspy was used to perform the decomposition and quantification of the elements in the spectral factors. **Supporting Fig. S23:** Nomenclature used for compositions at different length scales. Here the scale is being named based on transverse length (z-direction) which is in plane direction. Mesoscale compositions are measured by SEM-EDX while nanoscale and atomic scale compositions were measured by HR-STEM-EDX. **Supporting Fig. S24:** A) First negative scan (50 mV/s at 2500 RPM) on Glassy carbon in the presence of different metal cations (monometallic deposition) while B) shows the third negative scan (50 mV/s at 2500 RPM). Here it can be observed that onset potential decreases in the third scan, suggesting a seeding effect aiding in the deposition. **Supporting Table S1:** Comparing the Electrodeposition synthesis method with other reported synthesis method by comparing the estimated time of preparing 100 different compositions of HEA NPs on GC surfaces. An assumption is made to synthesize/transfer the different composition of NPs on GC so that the conventional electrochemical screening can be done. Here, the steps which are common in all synthesis methods like cleaning crucibles, glass-wares, GC surfaces, preparing precursors solutions are not incorporated due to lack of objectivity in the discussion of the reports. Sample preparation and sample transfer are key steps which brings a clear difference in the duration of preparing 100 different compositions. Moreover, parallel synthesis of different compositions is excluded from the discussion as it is a resource limited approach and is subject to specific labs<sup>1-9</sup>. **Supporting Table S2:** Bulk electrolyte compositions (molar fraction) of different samples synthesized on glassy carbon. For each composition, total concentration of precursors being 500 mM in the electrolyte and potentials used were  $E_{\text{nucleation}} = -0.15 \text{ V}_{\text{RHE}}$  ( $-0.50 \text{ V}_{\text{Ag/AgCl}}$ ),

$E_{\text{deposition}} = -0.10 \text{ V}_{\text{RHE}}$  ( $-0.45 \text{ V}_{\text{Ag/AgCl}}$ ) and  $E_{\text{rest}} = 1.15 \text{ V}_{\text{RHE}}$  ( $0.75 \text{ V}_{\text{Ag/AgCl}}$ )  $0.75 \text{ V}_{\text{Ag/AgCl}}$  with  $Rt = 1.0$  for 90 sec. **Supporting Table S3:** Mesoscale average (global) EDX compositions of various samples prepared from the bulk compositions mentioned in Supporting Table 2. Aitchison mean is used as the mesoscale average and calculated using the geometric mean of the element in a compositional data of a sample and then normalized with the sum of geometric means of all elements present in that sample. Compositions of NPs synthesized are quantified by using SEM-EDX equipped within Zeiss Gemini SEM 450. **Supporting Table S4:** Standard deviation (Std) in the mesoscale EDX compositions of various samples prepared from the bulk compositions mentioned in Supporting Table 2. **Supporting Table S5:** List the average particle size (weighted\_mean in nm) and the standard deviation (weighted\_std in nm) of the synthesized samples in S2 as per the bulk electrolyte composition. A watershed algorithm is used for segmentation after Otsu's thresholding for each tagged image file format collected from Gemini SEM 450. Further weighted average size and the weighted standard deviation is calculated as per the number of particles detected (# particles). # images indicates how many SEM images were analysed. **Supporting Table S6:** Diffusion adjusted compositions of different samples calculated by 'B/z' multiplication to the bulk electrolyte compositions and then calculating the molar fractions which are mentioned for all the bulk electrolyte compositions mentioned in Supporting Table 2. **Supporting Table S7:** Compositional distances (after Centered log-ratio transformation) calculated between mesoscale average compositional data mentioned in Supporting Table 4 and Bulk electrolyte data tabulated in Supporting Table 2 and diffusion adjusted data listed in Supporting Table 3. **Supporting Table S8:** List of the samples (bulk electrolyte compositions) used for mesoscale compositional analysis in Figure 6. **Supporting Table 9:** List of the samples used for nanoscale compositional analysis in Figure 6.